



HAL
open science

Rotor performance enhancement through blade surging

Tarek Bensebaa, Thierry Jardin, Sébastien Prothin, Nicolas Doué

► **To cite this version:**

Tarek Bensebaa, Thierry Jardin, Sébastien Prothin, Nicolas Doué. Rotor performance enhancement through blade surging. *International Journal of Micro Air Vehicles*, 2019, 11, pp.1-7. 10.1177/1756829319844275 . hal-03041153

HAL Id: hal-03041153

<https://hal.science/hal-03041153>

Submitted on 4 Dec 2020

HAL is a multi-disciplinary open access archive for the deposit and dissemination of scientific research documents, whether they are published or not. The documents may come from teaching and research institutions in France or abroad, or from public or private research centers.

L'archive ouverte pluridisciplinaire **HAL**, est destinée au dépôt et à la diffusion de documents scientifiques de niveau recherche, publiés ou non, émanant des établissements d'enseignement et de recherche français ou étrangers, des laboratoires publics ou privés.



Open Archive Toulouse Archive Ouverte (OATAO)

OATAO is an open access repository that collects the work of some Toulouse researchers and makes it freely available over the web where possible.

This is a publisher's version published in: <https://oatao.univ-toulouse.fr/27055>

Official URL : <https://doi.org/10.1177%2F1756829319844275>

To cite this version :

Bensebaa, Tarek and Jardin, Thierry and Prothin, Sébastien and Doué, Nicolas Rotor performance enhancement through blade surging. (2019) International Journal of Micro Air Vehicles, 11. 1-7. ISSN 1756-8293

Any correspondence concerning this service should be sent to the repository administrator:

tech-oatao@listes-diff.inp-toulouse.fr

Rotor performance enhancement through blade surging

T Bensebaa, T Jardin , S Prothin  and N Doue

International Journal of Micro Air

Vehicles

Volume 11: 1–7

© The Author(s) 2019

Article reuse guidelines:

sagepub.com/journals-permissions

DOI: 10.1177/1756829319844275

journals.sagepub.com/home/mav



Abstract

This short paper introduces a new concept of rotor where the blades undergo a periodic surging motion in the rotor disk plane. It is shown that the unsteady actuation induces aerodynamic phenomenon that can enhance both rotor thrust and efficiency, depending on the amplitude and frequency of actuation. In particular, the increase in aerodynamic performance is found to correlate with the development of a large scale leading edge vortex. Accordingly, the optimal frequency is found to correlate with the formation time of this vortex.

Keywords

Unsteady aerodynamics, surging rotor, leading-edge vortex

Received 1 March 2018; accepted 18 March 2019

Introduction

Unsteady airfoils can experience aerodynamic loads that are an order of magnitude larger than their steady counterparts. This was shown by Gursul and Ho¹ who experimentally measured the lift generated by a 20° pitch angle NACA0012 airfoil subjected to a sinusoidally varying freestream with velocity $U = U_\infty(1 + \sigma \cos(2\pi ft))$, where U_∞ is the average velocity and $\sigma \times U_\infty$ and f are the amplitude and frequency of the streamwise oscillation, respectively. The authors demonstrated that for an optimum reduced frequency $k = \pi fc / U_\infty$, and at a pitch angle that exceeds the static stall angle of the airfoil, a large leading edge vortex (LEV) was formed that, although shed, remained close to the wing surface for a large portion of the oscillation cycle, hence producing large lift. Simple theoretical considerations based on the wavelength of the vortex suggest that the optimal reduced frequency k should be on the order of 1,¹ which was verified by these experiments and other subsequent investigations.^{2–4} Overall, these findings echo extensive research on dynamic stall phenomenon.⁵

Based on these findings, we introduce in this short paper a very simple, yet new concept of a micro air vehicle's (MAV) rotor that aims at taking advantage of the aerodynamic mechanisms described above. The idea simply relies on operating the rotor at a rapidly varying rotation speed rather than at constant rotation

speed. The term 'surging rotor' is employed to reflect the surging motion of the blade (in the rotor disk plane) in the reference frame associated with the mean rotation speed. The aerodynamic performance of the surging rotor is investigated through resolution of the Unsteady Reynolds Averaged Navier–Stokes (URANS) equations. The results presented for various surging amplitudes and frequencies under hovering conditions show that a surging rotor can outperform a conventional rotor in terms of both rotor thrust and efficiency.

Numerical setup

The surging rotor consists of two untwisted rectangular blades with 4% thickness flat plate profiles. The blades have an $R = 5c$ span with a $1c$ root cut out, where c is the blade airfoil chord. The rotation speed of the rotor is $\omega = \omega_r(1 + \sigma \sin(\omega_s t))$, where ω_r and ω_s are the

Institut Supérieur de l'épéierforma et de l'épéieru (ISAE-Supaero),
Université de Toulouse, Toulouse, France

Corresponding author:

T Jardin, Département Aérodynamique Énergétique et Propulsion,
Institut Supérieur de l'épéieru, ue et de l'épéieru (ISAE-Supaero), 31400
Toulouse, France.

Email: thierry.jardin@isae.fr



average rotation speed and surging angular speed, respectively, and $\sigma\omega_r$ is the surging amplitude. The reduced frequency associated with the surging motion depends on the local radius r along the blade and can be expressed as $k(r) = \pi f_s c / \omega_r r = \omega_s c / 2\omega_r r$. Alternatively, one can define a global reduced frequency based on the velocity at 75% of the blade radius R , $k_R = 2\omega_s c / 3\omega_r R$.

The three-dimensional (3D) URANS equations are solved under their incompressible form using a finite volume method.⁶ An overset grid approach is used that allows each blade mesh to move following prescribed, sinusoidal rotating motions within a stationary background mesh. The structured mesh consists of 4.7 million hexahedral cells (0.9 million for each blade mesh and 2.9 million for background mesh) enclosed within a parallelepipedic domain of width $20R$ and height $50R$ (see Figure 1). The boundary conditions upstream and downstream of the rotor are implemented as pressure Dirichlet conditions, while the periphery of the parallelepipedic domain is defined using a slip-wall condition. The blades are modelled as non-slip surfaces. Blade mesh is moved with a time step smaller than $1/720$ time the rotating period. Both spatial and temporal discretizations are achieved using second-order schemes. Momentum and continuity equations are solved in an uncoupled manner using a predictor-corrector approach. Specifically, a colocated variable arrangement and a Rhie-and-Chow-type pressure-velocity coupling combined with a SIMPLE-type algorithm are used.^{7,8} Finally, the Spalart-Allmaras model⁹ is employed for URANS turbulence closure with maximum y^+ values on the order of 1.

Results for constant rotation speed cases are compared with available experimental data obtained at a Reynolds number of 60,000 (see Jardin et al.¹⁰ for details on the experimental approach). Figure 2 shows that experimental data match the mean rotation torque \bar{Q} versus mean thrust \bar{T} curve computed using the present numerical approach within reasonable accuracy. It should be noted that the present URANS approach considers the flow as fully

turbulent, which might not be the case at low Reynolds numbers typical of MAVs where laminar-to-turbulent transition may occur at a non-negligible distance away from the leading edge. Yet, transition may have an important role on the onset of flow separation along blade airfoil chord, hence on aerodynamic performance. However, the present blade geometry has a sharp leading edge which fixes flow separation at the leading edge and hence makes it less sensitive to turbulence modelling. In addition, the flow past a rotor blade is characterized by interactions between the blade and the wake from the previous blade, which promotes laminar-to-turbulent transition. Both properties (fixed separation and blade-wake interactions) contribute to the robustness of the numerical approach.

Furthermore, it was verified that the results are converged with respect to both spatial and temporal resolutions. Specifically, computations were conducted for

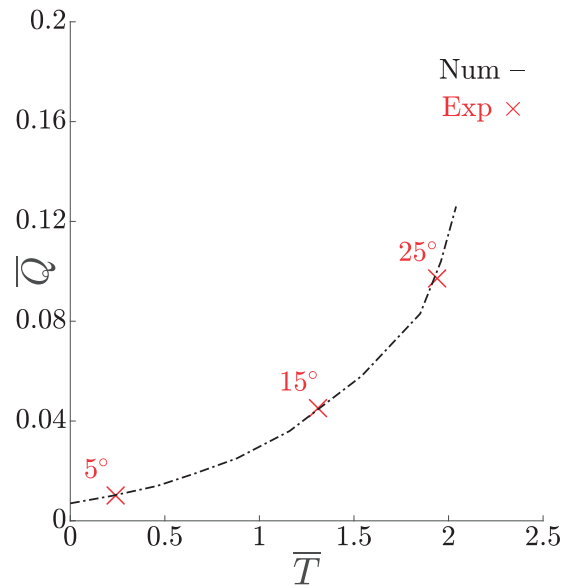


Figure 2. \bar{Q} (N.m) versus \bar{T} (N) map obtained numerically and experimentally for constant rotation speed cases at a Reynolds number of 60,000 (blade pitch angle is indicated on the graph).

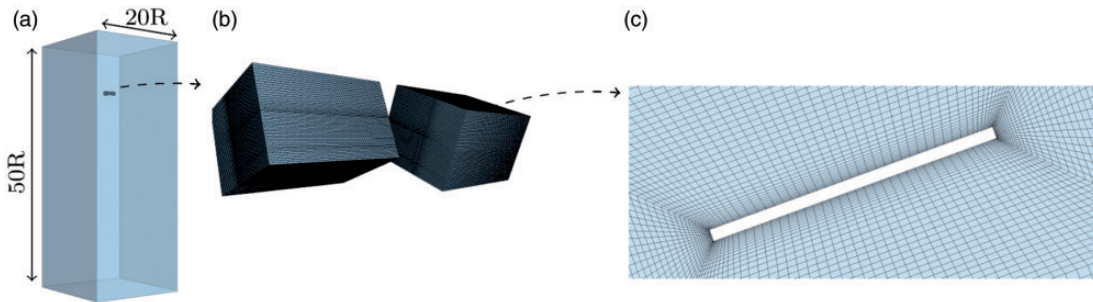


Figure 1. Parallelepipedic computational domain (a), overset blade mesh (b) and close-up view of the cross-sectional blade mesh (c).

both pitching and non-pitching rotors (15° mean pitch angle) with increased spatial and temporal resolutions (9 million cells and time step equal to $1/1440$ time the rotating period). Results demonstrated that increased resolutions yielded variations in both time-averaged thrust and torque lower than 2% of the reference values (i.e. those obtained with the present setup). Further details on these convergence tests can be found in Jardin et al.¹¹

In what follows, the results will be analysed in terms of mean rotor thrust coefficient \bar{C}_T and mean figure of merit $\bar{F}\bar{M}$, as defined in Leishman.¹² These quantities are obtained by non-dimensionalizing the mean thrust \bar{T} and power \bar{P} of the rotor such that $\bar{C}_T = \bar{T}/\rho A \omega_r^2 R^2$, $\bar{C}_P = \bar{P}/\rho A \omega_r^3 R^3$ and $\bar{F}\bar{M} = \bar{C}_T^{3/2}/\bar{C}_P \sqrt{2}$, where ρ is the fluid density and $A = \pi R^2$ is the rotor disk area. Recall that $\bar{F}\bar{M}$ is a non-dimensional measure of the efficiency of the rotor. It compares the power consumption of the rotor to that of an ideal rotor that would operate in a non-viscous flow (for which $\bar{F}\bar{M}$ equals unity) – hence $\bar{F}\bar{M}$ for a real rotor is always below 1. That is, $\bar{F}\bar{M}$ can be viewed as a measure of viscous losses in the flow.

Values of k_R and σ in the range (0.2–1.1) and (0.4–0.8) are considered, respectively. ω_r is set such that the Reynolds number at the tip of the blade is equal to $Re = \omega_r R c/\nu \approx 12,000$, i.e. typical of MAVs.

Results

Figure 3(a) shows the mean thrust coefficient \bar{C}_T as a function of the reduced frequency k_R for three surging amplitudes $\sigma = 0.4, 0.6$ and 0.8 . The blade pitch angle is here set to 15° , which is the pitch angle that leads to the highest $\bar{F}\bar{M}$ value when the rotation speed is constant,¹¹ i.e. $\sigma = 0$. The dashed line indicates the value of \bar{C}_T obtained in this constant rotation speed case. First, it can be seen that for a given σ , \bar{C}_T is maximized when $k_R = 0.8$. This optimal k_R value appears to be independent of σ . Note that $k_R = 0.8$ corresponds to $\omega_s/\omega_r = 6$. That is, six surging oscillations are completed during one rotating period. Second, it can be seen that for a given value of k_R , \bar{C}_T increases with σ . The increase in \bar{C}_T with respect to the constant rotation speed case reaches approximately 60% when $k_R = 0.8$ and $\sigma = 0.8$. Interestingly, the trends in \bar{C}_T with respect to k_R and σ and the optimal k_R value are in line with results obtained on nominally two-dimensional (2D) airfoils.¹ This suggests that, in our cases, the aerodynamics can be considered as quasi-2D in that 3D rotational effects (centrifugal and Coriolis accelerations, spanwise gradients in wing speed) do not fundamentally alter the flow physics revealed on 2D airfoils.

While a significant enhancement in lift is observed, Figure 3(b) shows that $\bar{F}\bar{M}$ is reduced when compared

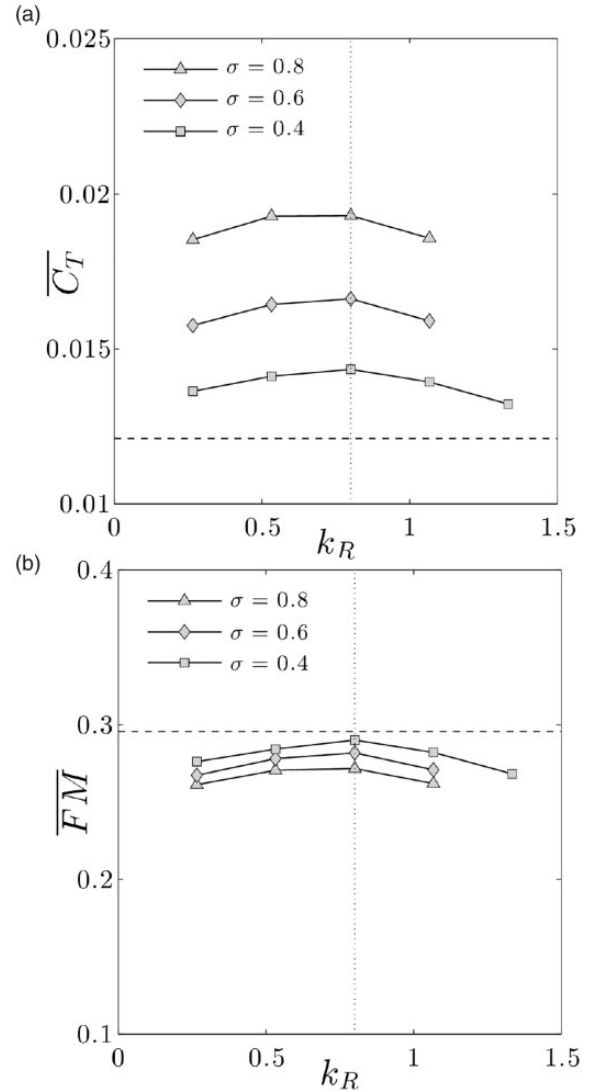


Figure 3. \bar{C}_T (a) and $\bar{F}\bar{M}$ (b) as a function of k_R obtained for a blade pitch angle of 15° on a rectangular planform.

to the value obtained in the constant rotation speed case. Again, it can be seen that for a given σ , $\bar{F}\bar{M}$ reaches a maximum at $k_R = 0.8$ and that for a given k_R , $\bar{F}\bar{M}$ decreases with σ . The reduction in $\bar{F}\bar{M}$ is however weak at low amplitudes when compared with the gain in \bar{C}_T . For example, the $k_R = 0.8$ and $\sigma = 0.2$ case exhibits an 18% increase in \bar{C}_T with respect to the constant rotation speed case, with a decrease in $\bar{F}\bar{M}$ below 2%.

Figure 4(a) and (b) displays similar results for a blade pitch angle of 20° . Similar conclusions than those raised for the 15° case can be made regarding the influence of surging amplitude and frequency on the aerodynamic performance of the rotor. However, it can be seen that in some specific cases, both \bar{C}_T and $\bar{F}\bar{M}$ can be increased with respect to the constant rotation speed case (e.g. $\sigma = 0.4$). In addition, the increase

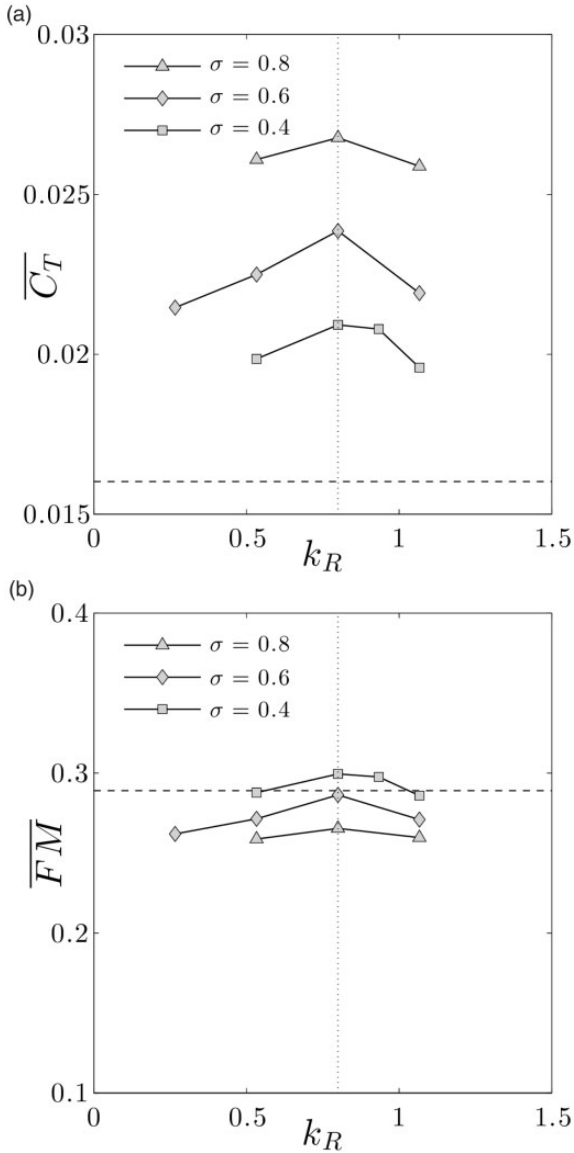


Figure 4. $\overline{C_T}$ (a) and \overline{FM} (b) as a function of k_R obtained for a blade pitch angle of 20° on a rectangular planform.

in \overline{FM} can be such that it exceeds the maximum \overline{FM} value reached in the absence of surging motion (which we remind is obtained for a 15° pitch angle). In other words, unsteady effects appear to be beneficial to rotor aerodynamic performance when the surging amplitude and frequency are set to appropriate values.

To quantify unsteady effects, the unsteady thrust coefficient C_T is compared to its quasi-steady counterpart for the $k_R = 0.8$ and $\sigma = 0.6$ case, with a 20° pitch angle. The quasi-steady thrust is obtained by computing the thrust of the rotor at different constant rotation speeds that correspond to instantaneous rotation speeds reached by the rotor at given instants during the surging period. In particular, five constant rotation speed cases allow us to determine the quasi-steady

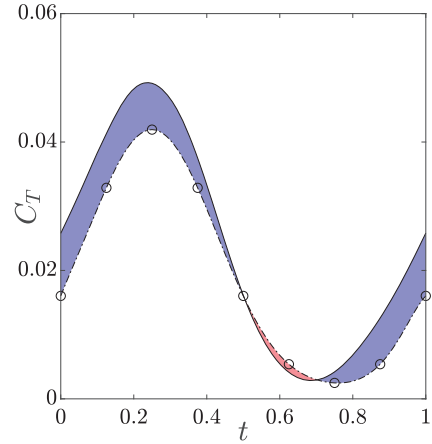


Figure 5. Unsteady (black line) and quasi-steady (black circles) thrust C_T as a function of time (non-dimensionalized by the surging period) obtained for the $k_R = 0.8$ and $\sigma = 0.6$ case, with pitch angle 20° . Blue and red regions represent beneficial and detrimental unsteady effects, respectively.

thrust at 0, 0.125, 0.25, 0.375, 0.5, 0.625, 0.75, 0.875 and 1 time the surging period. These values are plotted as black circles on Figure 5 where thrust is plotted as a function of time non-dimensionalized by the surging period. A polynomial fit (dash-dotted line) is superimposed on the graph and the difference with the unsteady thrust (black line) is filled with blue and red colours when unsteady effects are beneficial and detrimental to thrust, respectively. It is clearly shown from Figure 5 that unsteady effects are beneficial to thrust during most of the surging period. The only portion of the period where unsteady thrust is lower than quasi-steady thrust extends from $t = 0.5$ to $t = 0.7$, which corresponds to the early phase where the instantaneous rotor speed gets lower than the mean rotation speed.

This enhancement in instantaneous thrust can be correlated with the development of a large scale LEV that forms on the upper surface of the blade. Figure 6 shows a time sequence of the flow structure every $1/10$ th of the surging period. Vorticity contours and λ_2 -criterion isolines are shown in three cross-sections located at $1/4$, $1/2$ and $3/4$ span. At $t = 0$, the instantaneous rotation speed is equal to the mean rotation speed. Inception of an LEV is observed in the vicinity of the leading edge, on the upper surface of the airfoil. This LEV then develops as the rotation speed increases, reaching a conical shape with apex at the blade root. At $t = 0.3$, while the LEV covers only a small portion of the blade at the $1/4$ span location, it extends to the trailing edge at the $3/4$ span location. At $t = 0.4$ and $t = 0.5$, the LEV at the $3/4$ span location appears to lift off the surface and eventually sheds into the wake during the second half of the surging period. Further inboard (at $1/2$ and $1/4$ span), the LEV shedding also

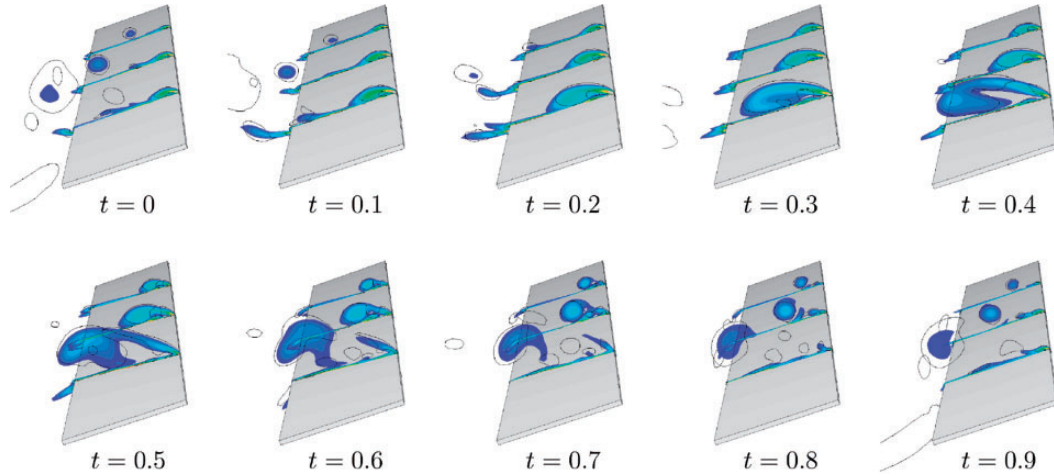


Figure 6. Cross-sectional spanwise vorticity contours and λ_2 -criterion isolines obtained for $k_R = 0.8$ and $\sigma = 0.6$ and with pitch angle 20° . Snapshots are displayed every $1/10$ th of surging period in the sections located at $1/4$, $1/2$ and $3/4$ span.

occurs but at slightly later times, i.e. around $t = 0.7$. Thus, at the $3/4$ span location, shedding coincides with both the LEV interacting with the trailing edge and the blade decelerating to rotation speed below the mean rotation speed, that is, the surging period can be correlated with the formation time of the LEV, at the $3/4$ span location. Conversely, further inboard, LEV shedding is triggered by blade deceleration before it can develop over the full chord and interact with the trailing edge. Here, the surging period is much smaller than the formation time of the LEV. Then, as the LEV is shed, another LEV forms at the leading edge of the airfoil. These observations show that the optimal surging frequency is the one that correlates with the formation time of the LEV around the $3/4$ span, i.e. where most of the aerodynamic forces are generated. Formation of the LEV in this section corresponds to beneficial unsteady effects on lift and shedding corresponds to detrimental effects.

Overall, these results demonstrate that a surging rotor can outperform a conventional rotor in terms of both thrust and efficiency. In addition, because the performance enhancement is associated with a well-defined time scale, it is possible to design a blade that better takes advantage of the mechanisms at play. In particular, it was mentioned that the reduced frequency $k(r)$ depends on the local radius along the blade. Therefore, in the case of blades with rectangular planforms where the chord is constant, $k(r)$ cannot be optimized in every blade sections. In fact, only one blade section operates in the optimal surging regime. To tackle this, the chord law can be designed such that, for a given configuration, $k(r)$ is constant along the blade. Thus, the local chord $c(r)$ should be equal to $2K\omega_r r/\omega_s$, where K is an arbitrary constant. For a given configuration, ω_r/ω_s is constant and therefore

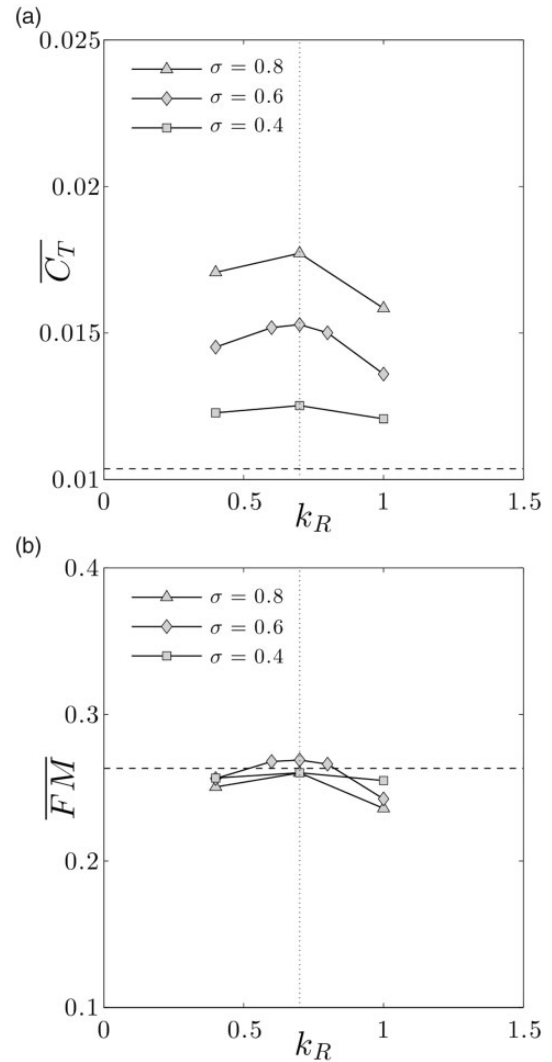


Figure 7. \bar{C}_T (a) and \bar{FM} (b) as a function of k_R obtained for a blade pitch angle of 15° on a trapezoidal planform.

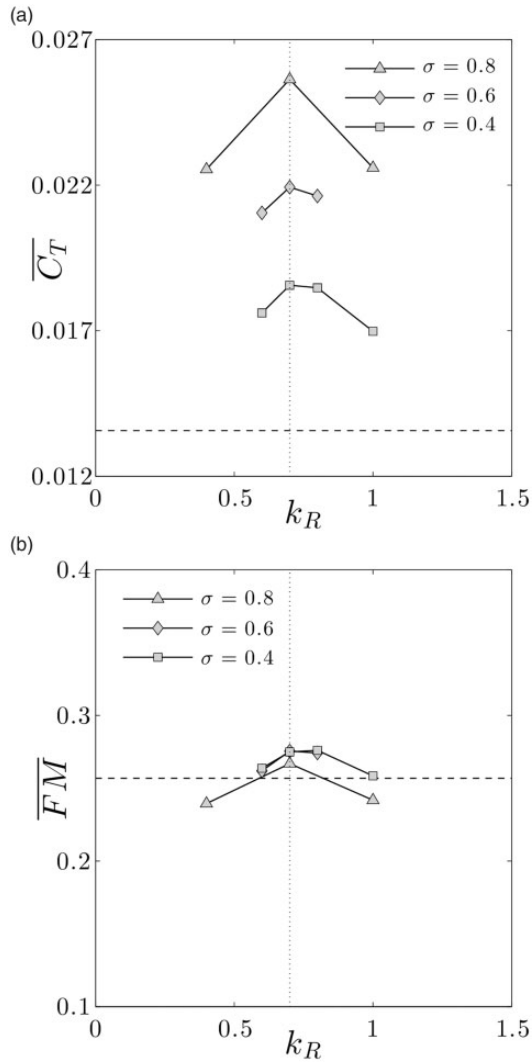


Figure 8. \bar{C}_T (a) and $\bar{F}M$ (b) as a function of k_R obtained for a blade pitch angle of 20° on a trapezoidal planform.

$c(r) = K'r$, where $K' = 2K\omega_r/\omega_s$, which suggests a trapezoidal planform.

In light of this, the previous analysis is reiterated using blades of trapezoidal planform, with chord distribution $c(r) = r/5$. Figures 7 and 8 show \bar{C}_T and $\bar{F}M$ obtained for both 15° and 20° pitch angles. Here again, the dashed lines indicate the values obtained in the constant rotation speed case. It is important to mention that the definition of aerodynamic coefficients is such that the blade surface is not taken into account (only the rotor disk area is taken into account, which is the standard way of non-dimensionalizing data in the literature). Therefore, coefficients for the trapezoidal planform are inherently lower than those obtained for the rectangular planform (the blade surface of the trapezoidal planform case is 1.6 times smaller than that of the rectangular planform case). Comparison between both planforms should be made taking into account the blade surface.

It can be seen from Figures 7 and 8 that both thrust and efficiency can be enhanced in a more significant amount than that obtained for the rectangular planform cases. In particular, both 15° and 20° cases lead to an increase in both \bar{C}_T and $\bar{F}M$ at the optimal frequency $k_R = 0.7$. Note that the optimal reduced frequency is slightly lower than that obtained for the rectangular planform cases, which is a simple artefact of the arbitrary reference length scale (here, 75% of the radius) used for the non-dimensionalization of k_R (in the trapezoidal planform case, the value of k_R is independent of this length scale because $c(r)/r$ is constant). For a 20° pitch angle, the increase in \bar{C}_T and $\bar{F}M$ with respect to the constant rotation speed case can reach approximately 62% and 7%, respectively ($\sigma = 0.6$ and $k_R = 0.7$), which further supports the idea that rotor

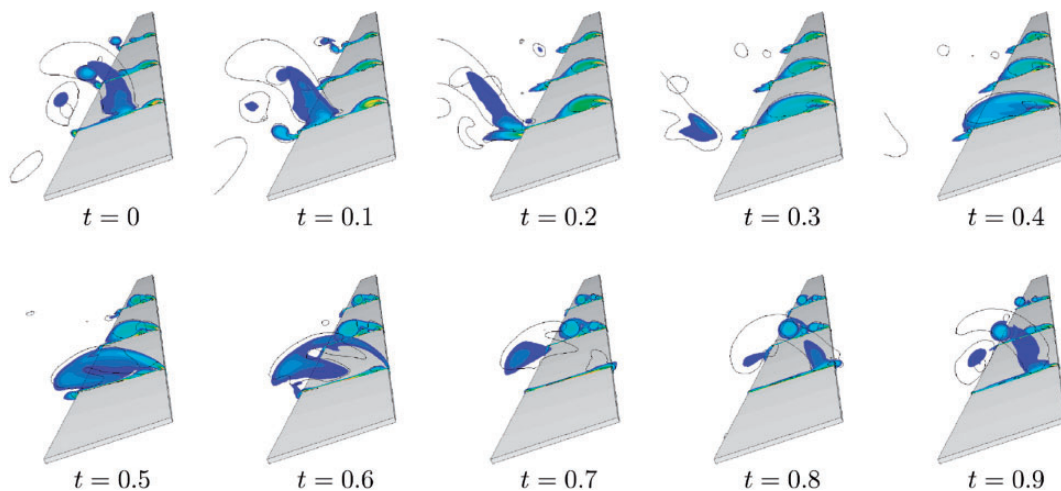


Figure 9. Cross-sectional spanwise vorticity contours and λ_2 -criterion isolines obtained on a trapezoidal planform for $k_R = 0.7$ and $\sigma = 0.6$ and with pitch angle 20° . Snapshots are displayed every $1/10$ th of surging period in the sections located at $1/4$, $1/2$ and $3/4$ span.

performance can be significantly enhanced through blade surging. Figure 9 shows a time sequence of the flow structure every 1/10th of the surging period. It can be seen that when the blade decelerates below the mean rotation speed, i.e. at $t=0.5$, the LEV covers the full blade chord in all three cross-sections. That is, the surging period can be correlated with the formation time of the LEV along the full span and the blade fully benefit from the development of the LEV to produce aerodynamic forces.

Conclusion and perspectives

In this short paper, a very simple, yet new concept of an MAV's rotor that aims at taking advantage of unsteady aerodynamic mechanisms induced by blade surging was introduced. It was shown that both rotor thrust and efficiency can be significantly enhanced for surging frequencies that correlate with LEV formation time. This correlation can only be obtained in a single radial section on a blade with rectangular planform but can be obtained all along the span for a trapezoidal planform, which thus better benefits from unsteady effects.

While the concept of 'surging rotor' reveals some interesting features in terms of aerodynamic performance, future studies are needed to understand its relevancy for MAVs' applications. In particular, rapid variation in rotor speed can be obtained with more or less complex solutions, such as variation of the motor speed, piezo-electric actuation or structural resonance. Variations of the motor speed at the optimal surging frequency (i.e. six times larger than the rotation frequency) could be easily implemented with off-the-shelf electronic speed controller (ESC) for typical rotation frequency on the order of 100 Hz, or alternatively, with dedicated ESC at higher frequencies. On the other hand, low amplitude, high frequency motions are well suited to the use of piezo-electric actuators, in this case involving a more complex system consisting, for instance, of stacked actuators at the blade hinge. The increase in power consumption due to rapid variation in rotor speed depends on the technology used to induce the surging motion; hence, tradeoffs between power consumption/complexity should be assessed. In addition, strong variations in aerodynamic loading induced by blade surging can be detrimental to flight

stability and control and induce strong aeroelastic effects.

Declaration of conflicting interests

The authors declared no potential conflicts of interest with respect to the research, authorship, and/or publication of this article.

Funding

The authors received no financial support for the research, authorship, and/or publication of this article.

ORCID iD

T Jardin  <http://orcid.org/0000-0001-9704-2984>

S Prothin  <http://orcid.org/0000-0002-5083-0892>

References

1. Gursul I and Ho C. High aerodynamic loads on an airfoil submerged in an unsteady stream. *AIAA J* 1992; 30: 1117–1119.
2. Gursul I, Lin H and Ho C. Effects of time scales on lift of airfoils in an unsteady stream. *AIAA J* 1994; 32: 797–801.
3. Granlund K, Monnier B, Ol M, et al. Airfoil longitudinal gust response in separated vs. attached flows. *Phys Fluids* 2014; 26: 027103.
4. Choi J, Colonius T and Williams D. Surging and plunging oscillations of an airfoil at low Reynolds number. *J Fluid Mech* 2015; 763: 237–253.
5. Carr L. Progress in analysis and prediction of dynamic stall. *J Aircr* 1988; 25: 6–17.
6. CD-adapco. *Star-ccm+ v11.02 user guide*. New York: CD-adapco, 2016.
7. Rhie C and Chow W. Numerical study of the turbulent flow past an airfoil with trailing edge separation. *AIAA J* 1983; 21: 1525–1532.
8. Ferziger J and Peric M. *Computational methods for fluid dynamics*. 3rd rev. ed. Berlin: Springer-Verlag, 2002.
9. Spalart P and Allmaras S. A one-equation turbulence model for aerodynamic flows. In: *AIAA 30th aerospace sciences meeting and exhibit: 0439*, 1992.
10. Jardin T, Prothin S and Magaña C. Aerodynamic performance of a hovering microrotor in confined environment. *J Am Helicopter Soc* 2017; 62: 1–7.
11. Jardin T, Doué N, Prothin S, et al. Numerical analysis of pitching-rotor aerodynamics. *J Fluids Struct* 2016; 62: 172–186.
12. Leishman G. *Principles of helicopter aerodynamics*. 2nd ed. Cambridge: Cambridge University Press, 2006.